JOURNAL OF PROPULSION AND POWER
Vol. 27, No. 2, March–April 2011

Optical Measurements of Neutral Cesium Mass Flow Rate in Field Emission Thrusters

Paul-Quentin Elias,* Denis Packan,* and Jean Bonnet*
ONERA, 91176 Palaiseau, France
Fabio Ceccanti,† Ugo Cesari,‡ and M. De Tata§
Alta SpA, 56121 Pisa, Italy
and
Davide Nicolini¶ and Eric Gengembre**
ESA, 2200 AG Noordwijk, The Netherlands

DOI: 10.2514/1.47830

Field emission electric propulsion thrusters using liquid cesium are currently being actively developed in Europe. For thruster–spacecraft interaction studies and design purposes, it is important to measure the mass flow rate of neutral cesium emitted by the thruster. This measurement requires the characterization of the neutral cesium plume. In this work, this characterization is achieved with a specially developed setup using laser-induced fluorescence velocimetry to probe the three components of the neutral cesium velocity and to measure the absolute number density from a field emission electric propulsion thruster representative of a flight model. The results give mappings of the plume velocity and number density along two planes intercepting the neutral plume for four different thruster operating conditions. Mass flow rates are obtained by integration of the local flow rates. The neutral cesium mass flow rate is in the milligrams/hour range; it increases with thrust and with emitter temperature. Mean neutral velocity can be as high as 800 to 1000 m s^{-1}. The results show that the neutral mass flow rate is of the same order of magnitude as the ion mass flow rate computed from the thruster current. This work provides the first direct measurement of neutral cesium mass flow rate, thruster efficiency, and, more generally, the first mapping of the neutral plume from this field emission electric propulsion thruster. The technique used could be extended to probe dimeric cesium in the plume.

Nomenclature

A	=	integral of the relative density profile, au
A_{21}	=	Einstein coefficient for spontaneous emission, s^{-1}
B_{21}	=	Einstein coefficient for stimulated absorption, s^{-1}
C_1	=	calibration coefficient for the first moment I^1, m^{-3} s^2
C_2	=	calibration coefficient for the second moment I^2, au
c	=	speed of light, m s^{-1}
$\mathrm{d}S$	=	elementary surface element, m^2
F	=	normalized velocity distribution function, m^{-3} s^3
f	=	normalized projected velocity distribution function, m^{-1} s
I	=	laser intensity, W m^{-2}
I_a	=	accelerator current, A
I_e	=	emitter current, A
I_{Sat}	=	saturation intensity, W m^{-2}
I^1	=	first moment of the fluorescence signal, s^{-2}
I^2	=	second moment of the fluorescence signal, s^{-3}
J	=	first moment of the transmission, s^{-1}
K	=	cesium number density integrated along the absorption line of sight, m^{-2}
k_T	=	proportionality constant for thrust-dependent mass flow rate, mg h^{-1} μN^{-1}
L_{Ref}	=	length of the reference cell, m
m_{Cs}	=	cesium atom mass, kg
n_{Cs}	=	cesium number density, m^{-3}
n_{Ref}	=	cesium number density in the reference cell, m^{-3}
q	=	cesium mass flow rate, mg h^{-1}
Q	=	quenching rate, s^{-1}
S	=	fluorescence signal detected, count s^{-1}
T	=	transmission coefficient
u	=	microscopic velocity, m s^{-1}
U	=	averaged velocity along a laser axis, m s^{-1}
V	=	probed volume, m^3
$\mathbf{V}$	=	averaged velocity vector in the laboratory coordinate system, m s^{-1}
V_a	=	accelerator voltage, V
V_e	=	emitter voltage, V
V_{ij}^z	=	averaged velocity along the Z axis, measured at node (i, j), m s^{-1}
Y	=	normalized line-shape function, s
η	=	deexcitation rate, s^{-1}
λ_0	=	transition wavelength, m
ν	=	frequency, MHz
ν_L	=	laser frequency, MHz
Ω	=	solid angle, sr

Subscript

Ref	=	reference quantity

Received 26 October 2009; revision received 23 August 2010; accepted for publication 8 September 2010.

*Research Scientist, Physics and Sensing Department; elias@onera.fr (Corresponding Author).
†Project Manager, Electric Propulsion; f.ceccanti@alta-space.com.
‡Head, Micropropulsion Laboratory, Electric Propulsion.
§Testing Engineer, Electric Propulsion.
¶LISA Pathfinder and Microscope Projects, Directorate of Science and Robotic Exploration; davide.nicolini@esa.int.
**Technical Officer, European Space Research and Technology Centre, Directorate of Technical and Quality Management; eric.gengembre@esa.int.

I. Introduction

THE concept of field emission electric propulsion (FEEP), with liquid cesium as a propellant, is very appealing for several

reasons. First, FEEP thrusters can cover a wide range of thrust, from submicronewtons to millinewtons. Second, they have a very good thrust resolution and near-instantaneous response capability. Third, they have a high specific impulse I_{sp} and thus require small amounts of propellant. These features make FEEP thruster very attractive for space missions, for which fine attitude control and drag compensation are required. This thruster is currently being developed and qualified for the ESA LISA (Laser Interferometer Space Antenna) Pathfinder mission to be launched in 2013.

The use of such thrusters on spacecraft requires a precise characterization of the thruster–spacecraft interaction; in particular, one should consider the effect of the neutral cesium emitted by the thruster. This neutral cesium emission has several detrimental effects. First, neutral cesium emission decreases the thruster I_{sp}. Second, the neutral cesium can contaminate the surface of the spacecraft. Third, via charge-exchange collision, it can lead to the production of slow ions that contribute to both thruster and spacecraft contamination and charging [1]. For all of these reasons, it is important to characterize this emission of neutral cesium. For this characterization, the neutral mass flow rate is the macroscopic parameter of primary interest; beyond the determination of this macroscopic parameter, which is crucial to compute the I_{sp}, the idea is also to measure the neutral plume divergence angle and to look for fast neutrals.

In the 1980s there were several efforts to measure the neutral mass flow rate on early versions of high-current cesium FEEP thrusters using a mass spectrometer [2] or direct measurements using a mass balance [3]. In the latter case, the differential weighing of the thruster gives the mass of propellant consumed per unit time. Subtracting the charged species mass flow (estimated from the emitted current) from this value, one obtains a figure for the total neutral cesium mass flow rate, which encompasses single atoms and dimers or heavier clusters. For a 10 mA current and 1.1 μm slit, the flow rate of neutral cesium (with no distinction between atomic cesium and clusters) represented about 30% of the total flow rate. Such a measurement could not be successfully done with the current version of the FEEP thruster, due to its much lower total flow rate (current less than 1 mA), which corresponds to a very small percentile mass consumption to be measured on the mass balance. In any case, this approach requires the knowledge of the cluster species in the beam from a mass spectrometer measurement or assumptions to match thrust measurements if available.

The particle flux measurements with a mass spectrometer done by Mitterauer [2] on an early FEEP thruster version could yield an estimate of the neutral cesium mass flow rate, with major assumptions though. In fact, mass spectrometer measurements are point measurements; thus, assumptions have to be made to obtain a mass flow rate from the measurement of the flux collected by the spectrometer at one location. In this case, it was found that the neutral mass flow rate of neutral cesium was in the microgram/hour range, no larger than 1% of the ion mass flow rate, by extrapolating the point measurements to the entire plume and comparing this with the measured total propellant flow rate.

These early measurements, although giving interesting orders of magnitude, do not provide a reliable measurement of the neutral cesium mass flow rate. Most important, though, was that they could not be reproduced on the current version of the thruster. They also support the idea that a full mapping of the neutral cesium plume is desirable to accurately measure the mass flow rate.

In this study, our goal is to obtain this mapping. For this purpose, we must use a nonintrusive diagnostic technique tool to measure the absolute number density and velocity vectors of the neutral cesium plume exiting the thruster, along control surfaces intercepting the plume. This technique is based on laser-induced-fluorescence Doppler velocimetry; it has been previously used to probe the axial velocity of xenon ions and neutrals from xenon Hall-effect thrusters [4,5]. However, a single component of the xenon ion velocity has been measured in these cases. Subsequently, efforts have been made to measure several velocity components: Hargus and Charles [6] and Hargus and Cappelli [7] have measured the axial and radial ion and neutral velocities in the plume of Hall-effect thruster, using two beams probing the plume in the axial and radial directions. Smith et al. [8] and Williams et al. [9] have developed three-beam laser-induced fluorescence (LIF) to measure all three components of the ion velocity vector, also in a Hall-effect thruster plume. They have used three parallel laser beams, focused at the same focal point by a converging lens. Thus, knowing the laser angles at the focal point, the three components of the velocity can be recovered. Although these studies have shown the feasibility of using multibeam LIF on plasma thruster, providing useful characterization of Hall-effect thruster plume, no macroscopic quantity (such as ion mass flow or thrust) could be retrieved from these data. In fact, in these studies, no simultaneous measurements of ion or neutral xenon number density have been performed. Such a measurement is a difficult task, because the ground state of Xe is in the vacuum UV [10]. To our knowledge, none have been performed concurrently with velocimetry measurements.

For cesium FEEP, the situation is quite different, because the ground-state transition lies in the near-infrared (IR) and can be probed directly using off-the-shelf laser diodes. Thus, in this study we perform three-beam LIF measurement combined with absorption measurement of cesium ground-state number density. This technique will be used to perform 2-D mappings in the thruster plume and yield the neutral cesium mass flow rate.

LIF involves the pumping of the excited states of a gas sample, using a tunable probing laser, and the subsequent observation of the fluorescence signal coming from the excited particles. In this work, the fluorescence signal comes from the deexcitation of the excited state of cesium, pumped directly from the ground state by a laser at 852 nm. As mentioned earlier, excitation originating from the ground state is an interesting feature, because it allows a direct calibration of the LIF by means of calibration cells containing cesium at known pressure. Once calibrated, the integral of the fluorescence signal is proportional to the neutral cesium number density. The frequency shift of the signal can be related, via the Doppler relation, to the velocity of the neutrals.

At the present time, the 3-D LIF diagnostic devised in this study is not intended to perform time-resolved measurements. Measurements were done on a thruster operating at steady state. Unexpected transients due to thruster sparking or emission site disturbances, both in the millisecond range, were smoothed out using a long acquisition time (a few seconds). In addition, we did not seek to retrieve the projected velocity distribution from the LIF, since only averaged velocities are required for mass flow rate measurements. We focused on the mapping of the neutral cesium number density and 3-D velocity vector on two planes located close to the exit plane of the thruster. The goal was to use these mappings to deduce the neutral mass flow rate from the thruster. To our knowledge, this is the first time such a complete characterization has been performed.

II. Background

A. Cesium-Fed FEEP Thruster

FEEP generates thrust by ionization of liquid metals and acceleration of the cesium ions by a strong electric field. Ionization occurs at the tip of the emitter electrode, which is wetted by the liquid cesium. An accelerator plate is placed in front of the emitter electrode, as shown in Fig. 1. When a high-voltage difference is applied between the emitter and the accelerator, the free surface of the liquid cesium is distorted and (above a certain threshold voltage) forms small cusps, at the tip of which the electric field is considerably enhanced. When the electric field reaches a value of about 10^9 V m^{-1}, atoms at the tip of the cusps are spontaneously ionized and an ion beam is extracted. This ion beam is then accelerated at kinetic energies of around 10 keV by the voltage drop, which generates the thrust.

In this study, an engineering model of a cesium-fed FEEP thruster was used. The thruster is representative of a flight model, in terms of thrust and thermal performance. It was modified to accommodate two viewports on its side; this gives an optical access just in front of the accelerator plate. Figure 1 presents a view of the thruster. Note

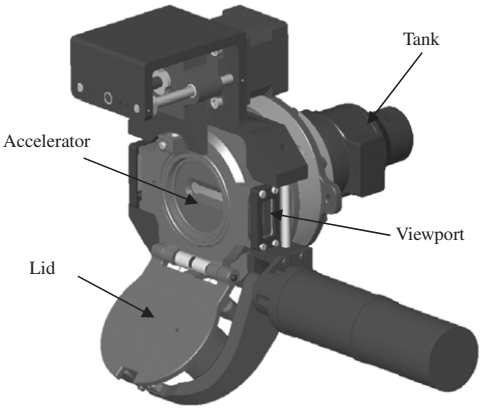

a) CAD view of the thruster used for the test

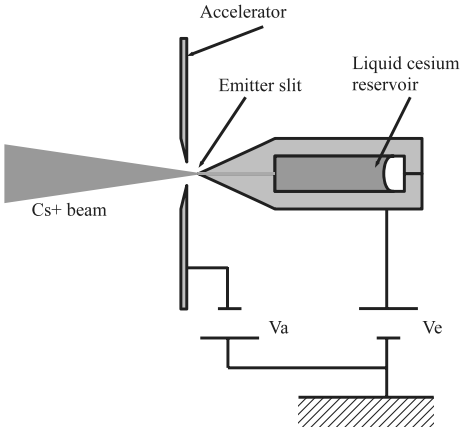

b) Schematic representation of the FEEP thruster

Fig. 1 Cesium-fed FEEP thruster.

that no beam neutralization device was used, because the thruster was tested in a facility-neutralized configuration.

The FEEP thruster was operated at two thrust values: 30 and 100 μN. These thrust values are the setpoints of the thruster. They are not measured; instead, they are computed from the ion current and emitter/accelerator voltages. Control of thrust is performed using emitter voltage V_e, while accelerator voltage V_a is kept constant. A closed-loop regulator controls the emitter voltage to maintain the product $(I_e - I_a)\sqrt{V_e}$ at a fixed value (depending on preset thrust level). The correlation between electrical parameters and actual thrust was performed in the frame of a dedicated test campaign, reported in [11], showing that the discrepancy between the theoretical model and actual measurement is between 10 and 20%, depending on thrust level. Accordingly, the nominal values of 30 and 100 μN in the following refer to an actual thrust of about 35 and 115 μN, respectively. When the thruster fires up, bright spots appear along the emitter tip. The higher the thrust, the more spots there are, as shown in Fig. 2.

B. Cesium Spectroscopic Properties

The transition that is of interest for us in neutral cesium is the so-called D2 transition at about 852 nm.[††] Historically, people have noticed its two key advantages: it is very intense and it starts from the ground state. The intensity ensures that excitation does not require prohibitively powerful light sources, and starting from the ground state ensures that the population representative of the bulk flow of atoms is probed. If one takes a transition starting from an excited state instead, only the small fraction of population in that excited state is probed. This would yield a low intensity of emission and absorption that would not be easily related to the actual number of atoms.

[††]Data available online at http://steck.us/alkalidata [retrieved 2010].

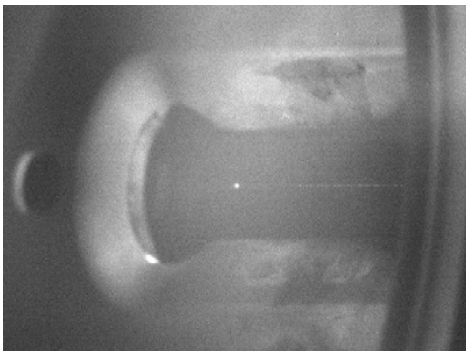

Thrust 40 μN

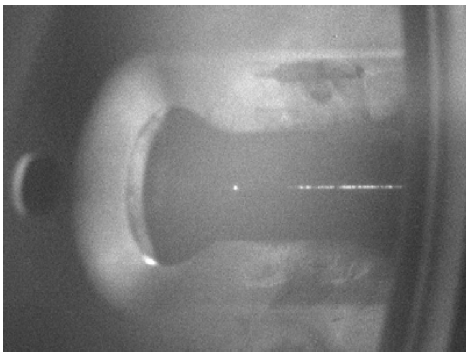

Thrust 100 μN

Fig. 2 View of the thruster emitter slit at 40 and 100 μN. At 40 μN, few emissive spots can be seen. At higher thrust (100 μN), the slit is almost continuously lighted by the emissive spots.

One other property is that the D2 transition is isolated: the upper state is radiatively linked only to the ground state. The energy levels and hyperfine splitting of the transition are shown in Fig. 3. Thus, it can be considered as close to an ideal two-state system. This and other properties made cesium desirable for use in atomic clocks, which resulted in numerous studies of the D2 transition, and its characteristics are now very well known. It also resulted in the availability of off-the-shelf lasers at its wavelength (about 852 nm). For all of these reasons, the D2 transition is ideal to make quantitative measurements on cesium atoms.

In our study, we focus on the three transitions bound to the $F = 4$ hyperfine level of the ground state. Their frequencies are given in Table 1.

C. LIF Theory

In a neutral cesium vapor, LIF is a diagnostic technique suitable for determining ground-state number density. As shown in Fig. 4, LIF diagnostic involves 1) the pumping of the neutral cesium initially in its ground state E_1 toward and excited state E_2 and 2) the collection of

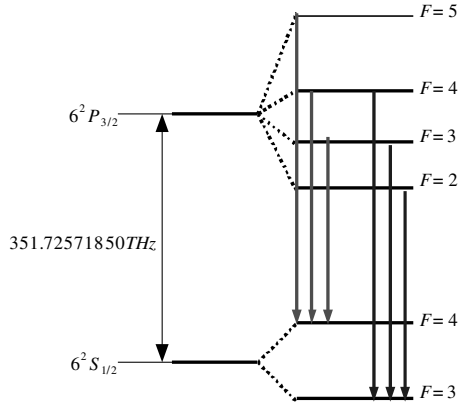

Fig. 3 Allowed transitions of the D2 line of neutral cesium.

Table 1 Frequencies from the $F = 4$ ground state

Upper state	Transition frequency, MHz
$F = 3$	$\nu_{34} = 351,721,508.284$
$F = 4$	$\nu_{44} - \nu_{34} = 201.42$
$F = 5$	$\nu_{54} - \nu_{34} = 452.24$

the fluorescence signal resulting from the spontaneous decay of the atom in its excited state toward the ground state.

Solving the LIF problem, i.e., relating the fluorescence signal to the ground-state number density, implies rate equations and thus a time-dependent problem. However, if the time of residence of the sampled population in the probing laser beam is greater than the pumping and fluorescence time, the steady-state solution can be considered. This is the case in our application, because the characteristic pumping time and fluorescence time are of a few tens of nanoseconds, whereas the residence time is in the microsecond range. Thus, the fluorescence signal detected is proportional to the deexcitation rate from the excited state at steady state.

Let us derive the expression for the detected signal. Let V be the volume defined by the crossing of the pumping laser beam and of the detection optic beam, and let Ω be the solid angle of the detection optic as seen from V. First let us consider a gas of cesium at rest; the fluorescence signal detected (in counts per second) is

$$S(\nu) = n_{\mathrm{Cs}} V \frac{\Omega}{4\pi} \eta \frac{I/I_{\mathrm{Sat}}(\nu)}{1 + 2I/I_{\mathrm{Sat}}(\nu)} \tag{1}$$

where $\eta = A_{21} + Q$ is the deexcitation rate, and

$$I_{\mathrm{Sat}} = \frac{A_{21} + Q}{B_{21} Y(\nu)}$$

is the saturation intensity of the transition, where Y is the normalized line shape of the transition, centered at $\nu_0 = c/\lambda_0$.

Second, in the case of a gas with a velocity distribution $F(u, v, w)$, because of the Doppler effect, the relative velocity of the gas with respect to the pumping laser changes laser frequency, as seen from the moving-gas frame of reference. Suppose that the laser beam is parallel to the x axis, then the normalized distribution of velocities parallel to the x axis, as seen from a pumping laser, is

$$f(u) = \iint F(u, v, w)\, \mathrm{d}v\, \mathrm{d}w \tag{2}$$

Thus, the fluorescence signal from the fraction of the gas with relative velocity u is

$$S_u(\nu) = n_{\mathrm{Cs}} f(u) V \frac{\Omega}{4\pi} \eta \frac{I/I^u_{\mathrm{Sat}}(\nu)}{1 + 2I/I^u_{\mathrm{Sat}}(\nu)} \tag{3}$$

where

$$I^u_{\mathrm{Sat}} = (A_{21} + Q_{21}) \Big/ \left(B_{21} Y\left(\nu - \frac{u}{\lambda_0} \right) \right)$$

is the shifted normalized line shape of the transition, centered at $\nu_u = \nu_0 + u/\lambda_0$. The total signal detected is the sum of contributions of the gas atoms in all velocity classes:

$$\begin{aligned} S(\nu) &= \int S_u(\nu)\, \mathrm{d}u \\ &= n_{\mathrm{Cs}} f(\lambda_0(\nu_0 - \nu)) \underbrace{\left[V \frac{\Omega}{4\pi} \eta \int \frac{I/I^u_{\mathrm{Sat}}(\nu)}{1 + 2I/I^u_{\mathrm{Sat}}(\nu)}\, \mathrm{d}u \right]}_{C} \end{aligned} \tag{4}$$

In deriving the right-hand side of Eq. (4), we assume that the saturation-broadened line shape

$$\frac{I/I^u_{\mathrm{Sat}}(\nu)}{1 + 2I/I^u_{\mathrm{Sat}}(\nu)}$$

is much narrower than the Doppler-broadened line shape $f(\lambda_0(\nu_0 - \nu))$. This allows one to take $f(\lambda_0(\nu_0 - \nu))$ out of the integral. This is true as long as the laser intensity is not too high (say, $I \leq 10 I_{\mathrm{Sat}}$), which is always the case in this study. By taking the moments of the LIF signal, one gets

$$I^1 = \int S(\nu)\, \mathrm{d}\nu = n_{\mathrm{Cs}} C_1 \tag{5}$$

$$I^2 = \int \mathrm{S}(\nu) \nu\, \mathrm{d}\nu = I^1 \frac{U}{\lambda_0} + I^1 C_2 \tag{6}$$

where $U = \int f(u)\, \mathrm{d}u$ is the mean gas velocity along the probing laser beam axis, and C_1 and C_2 are constants to be determined by an appropriate calibration. In our case, the problem is slightly more complex, because there are three different transitions that add their contribution to the total signal. The generalization is straightforward and will not be detailed here.

III. Principle of the Mass Flow Rate Measurement

To measure the neutral cesium mass flow rate q, it is necessary to integrate the mass flux $m_{\mathrm{Cs}} n_{\mathrm{Cs}} \mathbf{V}$ around a control surface enclosing the thruster:

$$q = m_{\mathrm{Cs}} \int_S n_{\mathrm{Cs}} \mathbf{V} \cdot \mathbf{n}\, \mathrm{d}S \tag{7}$$

The choice of the control surface is dictated by two criteria. First, to have an accurate measurement of the neutral mass flow rate, the control surface must intercept most of the neutral plume from the thruster. Second, flow measurements across two different surfaces allow cross-checking and thus increase the confidence in the results. For these reasons, two different control surfaces have been defined in the thruster coordinate system; in Fig. 5 a cross section of the thruster emitter shows the coordinate system arrangement. The slit lies in the $Z = 0$ plane, and the origin of the coordinates frame is at the center of the emitter slit.

The two different control surfaces probed intercept the whole plume. They are shown in Fig. 6. The surfaces chosen in the thruster coordinates are as follows:

1) The X–Y plane at $Z = 3$ mm (middle of the lateral view ports), named plane B, is just downstream of the accelerator plate.

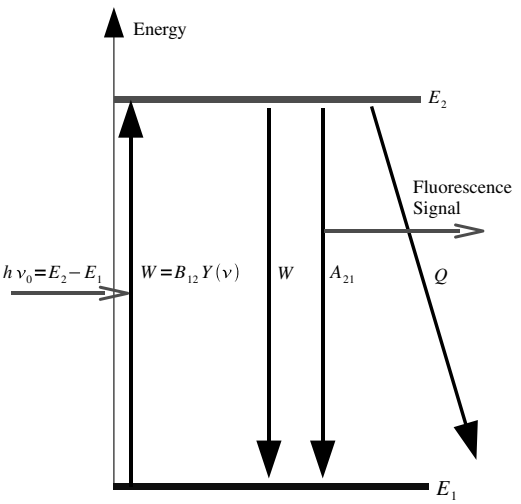

Fig. 4 Energy diagram of a two-state system. The pumping laser beam, when tuned, excites the atoms to E_2 at a rate W. The excited atoms then relax to their ground state E_1, due to natural decay or stimulated emission, or to another state, due to quenching, with rates A_{21}, W, and Q.

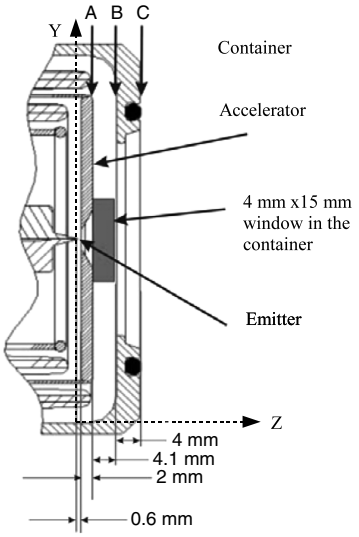

Fig. 5 Cross section of the thruster emitter, figuring the lateral window dimensions and the approximate Z positions of planes B and C.

2) The X–Y plane at $Z = 9$ mm (thruster exit plane), named Plane C, is on the thruster exit plane.

Each of these two planes intercepts virtually everything that exits the emitter slit. Thus, they will each measure the outflow of neutral cesium, and their measurements should be the same.

Since the three-component LIF Doppler technique used here can only perform point measurements, the integral in Eq. (7) is discretized by using a mesh of the control surface. As shown in Fig. 7, the control surface is a plane parallel to the X–Y plane. Thus, the mass flow rate across the control surface is approximated by measuring the number density n_{Cs} and V_{ij}^{Z} and the Z component of the velocity V_{ij}^{Z} at the nodes (i, j) on a mesh of the control surface, then using the approximate expression for Eq. (7):

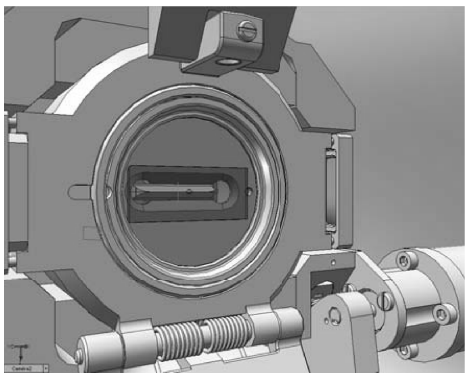

a) Plane B

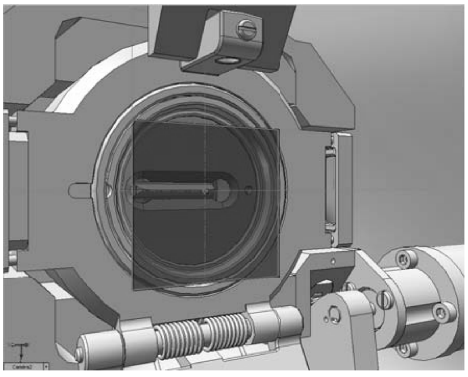

b) Plane C

Fig. 6 CAD view of planes B and C.

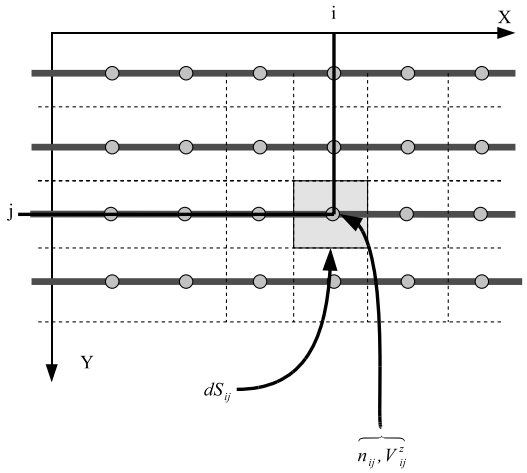

Fig. 7 View of the discretized control surface. LIF measurements give cesium number density and Z velocity at discrete location marked by (i,j) indices.

$$q = m_{\mathrm{Cs}} \sum_{i=1}^{NX} \sum_{j=1}^{NY} n_{ij} V_{ij}^{z} \, \mathrm{d}S_{ij} \tag{8}$$

On a given control surface, the velocity vectors at the nodes of the mesh are determined using LIF Doppler velocimetry; the number densities are measured using LIF calibrated with absorption measurements.

A. Three-Component Velocimetry Using LIF Doppler

A cloud of neutral cesium atoms moving at a speed u along the probing laser beam axis will have its fluorescence peak shifted by $\Delta\nu$, due to the Doppler effect:

$$\Delta\nu = \frac{u}{\lambda_0} \tag{9}$$

From this equation, we can see that the velocity measurement resolution is directly dependent on the frequency-shift measurement resolution. For example, if one wishes a velocity resolution of 10 m s^{-1}, which is necessary to resolve the thermal plume, then a frequency resolution of at least 10 MHz is required. To achieve this resolution, we calibrate the frequency of the tuned laser using the Doppler-free absorption spectrum in a reference cesium cell. The Doppler-free spectrum has peaks at the three transition frequencies of the D2 line and also at the midpoint between these transition

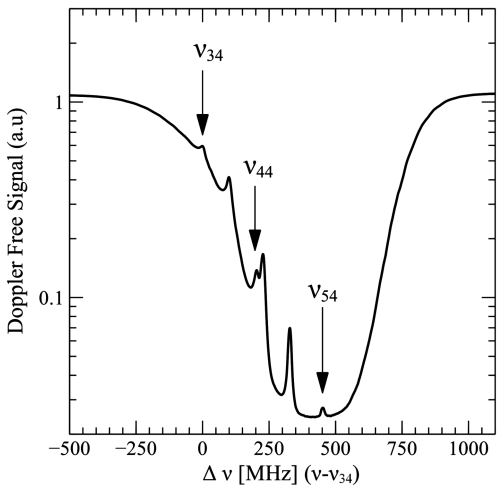

Fig. 8 Doppler-free absorption spectrum; the reference of the frequency axis is ν_{34}, as given in Table 1. Intermediate peak frequencies are precisely known and are also used to calibrate the laser frequency.

frequencies. The reason for that is that the Doppler-broadened absorption line has a width of about 380 MHz at room temperature, which is the same order of magnitude as, say, $\nu_{44} - \nu_{34}$. Thus, we count six peaks in the absorption spectra: three correspond to the transition frequencies given in Table 1, and three correspond to the midpoint frequencies $(\nu_{44} + \nu_{34})/2$, $(\nu_{54} + \nu_{34})/2$, and $(\nu_{44} + \nu_{54})/2$. An example of this Doppler-free spectrum is given in Fig. 8. While the laser diode scans the frequency axis, this spectrum can be used to accurately calibrate the frequency; the resolution is close to the natural linewidth and is below 10 MHz.

Once the frequency is calibrated, we can compute the second moment of the LIF signal, as given in Eq. (6), in which the mean velocity U along the laser axis appears. Suppose now that we also measured the LIF signal S_R from a reference cell containing neutral cesium at rest:

$$I^2_{\text{Ref}} = \int \text{S}_{\text{Ref}}(\nu)\nu \, \text{d}\nu = I^1_{\text{Ref}} C_2 \tag{10}$$

From this reference measurement we can compute the calibration coefficient C_2 and then obtain the mean velocity along the axis:

$$U = \lambda_0 \left(\frac{I^2}{I^1} - \frac{I^2_{\text{Ref}}}{I^1_{\text{Ref}}} \right) \tag{11}$$

Repeating LIF measurement in the same volume along three laser axes that form a trihedron yields three projections of the mean velocity U_1, U_2, and U_3. Noting $\mathbf{V}$ as the velocity vector expressed in the laboratory coordinate system,

$$\mathbf{V} = \begin{pmatrix} V^x \\ V^y \\ V^z \end{pmatrix}$$

Let $\mathbf{e_1}$, $\mathbf{e_2}$, and $\mathbf{e_3}$ be the unit vectors of the three laser beam axes. The projection of the velocity on axis i is given by

$$U_i = \mathbf{e}_i \cdot \mathbf{V} \qquad i = 1, 2, 3$$

This relationship can be cast in a matrix form, noting $U_{\text{Laser}} = (U_1 \quad U_2 \quad U_2)$ as the velocity vector in the laser beam coordinate system:

$$\mathbf{U}_{\text{Laser}} = \underbrace{\begin{pmatrix} e_{1x} & e_{1y} & e_{1z} \\ e_{2x} & e_{2y} & e_{2z} \\ e_{3x} & e_{3y} & e_{3z} \end{pmatrix}}_{\mathbf{A}} \begin{pmatrix} V^x \\ V^y \\ V^z \end{pmatrix}$$

Hence,

$$\mathbf{V} = \mathbf{A}^{-1}\mathbf{U}_{\text{Laser}} \tag{12}$$

The three components of the velocity vector in the thruster coordinate system U_x, U_y, and U_z are then recovered at the cost of a simple matrix multiplication. Note that to compute the mass flow rate, determining the mean velocity is sufficient; while computing I^2 to get U, any information on the velocity distribution is lost. In our case this is unimportant, as we focus solely on a macroscopic quantity.

B. Absolute Number Density Measurement Using LIF and Absorption

Calibrating the measurement to yield the absolute number density is equivalent to determining the proportionality factor C_1 in Eq. (5). There are two possibilities to obtain this factor:

1) Use a reference measurement at a known number density. This is doable using a calibration cell, with a known cesium vapor pressure placed directly at the laser beam crossing: i.e., in front of the thruster.

2) Use another absolute measurement and calibrate the LIF signal against this measurement. This is doable using an absorption measurement.

Option 1, although more straightforward and flexible by allowing a point calibration (whereas option 2 needs a whole line measurement to perform the calibration), has a big drawback. To accurately calibrate the LIF signal, we have to be sure that the laser intensity in the calibration cell is equal to the laser intensity during the measurement, as C_1 and C_2 in Eqs. (5) and (6) depend on the laser intensity. This is very difficult to obtain: first, because calibration cannot be performed at the same time as the measurement; indeed, the thruster needs to be off to use the calibration cell. The laser intensity is sensitive to the room temperature, and so it is difficult to guarantee a repeatable intensity level. Second, and more important, the calibration cell acts as an optical system on the laser beam, which modifies the focalization of the laser beam. Thus, the laser intensity, as seen from the collection optic line of sight, is changed. And indeed, calibration discrepancies have been observed with option 1 during tests.

For these reasons, option 2 has been chosen. The principle of this measurement is as follows: LIF signals are collected at discrete points along a line parallel to the X axis of the thruster, to get the relative density profile. Along this same line, an absorption measurement is performed. Let $T(\nu)$ be the transmission measured as a function of frequency. It can be shown [12] that

$$\int_0^\infty \ell_n(T(\nu_L))\, \text{d}\nu_L = \text{cst} \int n_{\text{Cs}}\, \text{d}x \tag{13}$$

The proportionality coefficient cst is independent of the laser intensity; it can be accurately measured using a reference absorption measurement T_{Ref} with the calibration cell of known number density n_{Ref} and length L_{Ref} placed in the probing beam while the thruster is off. Thus, we have

$$\int n_{\text{Cs}}\, \text{d}x = n_{\text{Ref}} L_{\text{Ref}} \frac{\int_0^\infty \ell_n(T(\nu_L))\, \text{d}\nu_L}{\int_0^\infty \ell_n(T_{\text{Ref}}(\nu_L))\, \text{d}\nu_L} \tag{14}$$

Let us define J as $J = \int_0^\infty \ell_n(T(\nu_L))\, \text{d}\nu_L$. Equation (14) can be rewritten as

$$K = \int n_{\text{Cs}}\, \text{d}x = n_{\text{Ref}} L_{\text{Ref}} \frac{J}{J_{\text{Ref}}} \tag{15}$$

Here, the spatial integration is performed between the emission and the collection optics of the absorption system.

The LIF measurement along the X line yields NX discrete measurements I^1 at positions x_i $(i = 1, \ldots, NX)$, as shown in Fig. 7. Measurement $I^1(x_i)$ is at position x_i, as shown in Fig. 9. Hence, we can write an estimate of the hatched area. This gives

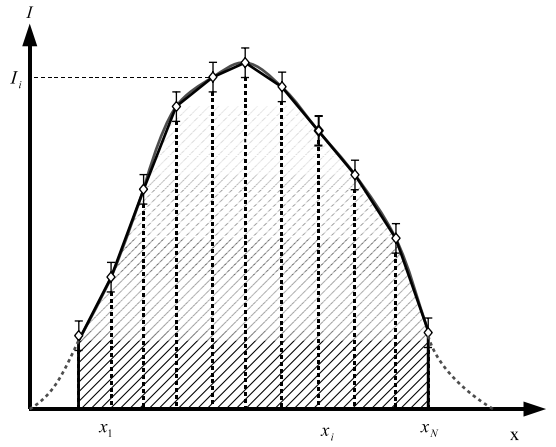

Fig. 9 Example of the numerical integration of a smooth function (in red) using the trapezoid method (hatched area). The relative profile is given by the measurements at points x_i, noted by circles. Note that the tails of the smooth function cannot always be resolved and thus have to be extrapolated.

$$A = \sum_{i=1}^{NX} \alpha_i I^1(x_i) \tag{16}$$

where the α_i are coefficients depending on the x_i, as given by the trapezoid method. Combining Eq. (16) with Eqs. (5) and (15), we obtain the following formula to calibrate the LIF signals:

$$C_1 = \frac{A}{K} \tag{17}$$

Using Eq. (17), we can determine the calibration coefficient C_1 for each line and thus, using Eq. (5), get the local cesium number density for each point measurement. Note that Eq. (17) supposes than the coefficient C_1 is the same for each point of the line. This coefficient depends nonlinearly on the laser intensity, on the probed volume, and on the saturation level. For this reason, all points are taken sequentially, once the diode is properly stabilized.

IV. Experiment Details

In the previous section we described all the conceptual elements required to compute the mass flow rate. To succeed in measuring the mass flow rate, we needed to design a setup that had the following features: 1) accommodation of a thruster firing 10 keV ions in good vacuum conditions, 2) probing at discrete points on all control surfaces, 3) calibration of the frequency using a Doppler-free absorption cell, 4) calibration in vacuo using a reference cell, and 5) laser probing along three axes.

A. Vacuum Tank Facility

We have used the B61 vacuum tank facility at ONERA laboratory, which was designed to accommodate electric thrusters. It is composed of two chambers. The test chamber, in which the thruster is mounted, is 0.6 m in diameter and 1 m in length. It can be isolated from the main chamber, which is 1 m in diameter for 4 m in length. The thruster is oriented to fire straight in the main chamber. The length of the main vessel reduces the problems due to sputtering by the ion beam. The vacuum tank is fitted with a turbomolecular pump and a cryopump, whose pumping speeds for cesium are 1000 and 7000 liters/second, respectively. However, adsorption of cesium on the tank walls probably led to a much higher effective pumping rate for cesium.

During these measurements, the background pressure in the vacuum tank is of the order of 10^{-7} mbar.

B. Experimental Setup

The setup is made of two sections: the first section generates and analyzes the laser beams, and the second section is composed of the optics and actuators in vacuum. One of the challenges of the experiment is that once the thruster is started, the vacuum cannot be broken, because it would lead to slit oxidation and end of life for the thruster. Thus, we had to make provision for alignment and calibration in vacuum (accounting for sputtering on the optics), and most of the optics are mounted on vacuum-rated actuated mounts. The experimental setup is sketched in Fig. 10 and is composed of three parts. The first part is the laser optical train, the second part is the test bench in the vacuum tank, and the third part is the detection stage.

The laser used is a TEC-500 tunable laser Diode from Sacher Lasertechnik. Its mode-hop-free tuning range is typically ± 20 GHz, centered at around 852 nm. The 10 mW beam goes through a Faraday isolator. A first beam pickoff is used for the Doppler-free absorption. A second beam pickoff is used to monitor the beam power. A third pickoff is used to obtain a reference LIF signal in a gas cell containing pure cesium with zero velocity. A temperature probe located at the surface of the cell is used to compute the vapor pressure in the cell. Then the beam is split into four beams. These beams are directed to the test bench in the vacuum tank, through 50 μm IR-grade optic fibers. Three of these beams are used for probing the plume along three axes. The fourth beam is used for the absorption measurement

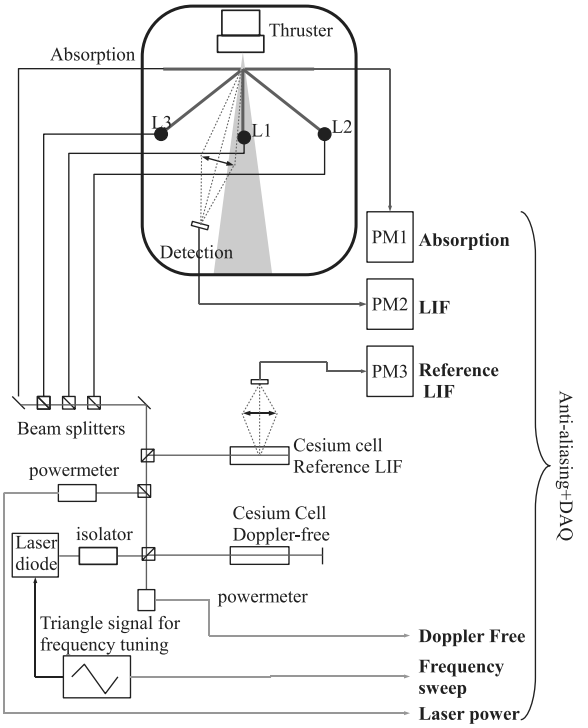

Fig. 10 Diagram of the experimental setup for three-component LIF measurements.

across the plume. The laser frequency is driven by a sawtooth-shaped sweep signal. The frequency range is swept up and down at 6 Hz.

The test bench located in the vacuum tank is shown in Fig. 11, with the thruster mounted on it. It is composed of three injection IR-grade aspherical lenses with diameter of 9.4 mm and focal length of 11 mm oriented to focus the three laser beams at the same spot. The three focusing beams from these optics (termed L1, L2, and L3) form a trihedron. It is important to measure this trihedron accurately in order to compute the velocity vector in the correct coordinate system. For this purpose, before installing the thruster, vectors e_1, e_2, and e_3 defining the laser trihedron have been measured using a flat plate placed parallel to the X–Y plane. By moving this plate along the Z axis by known increments and measuring the position of the laser beam impact, it is possible to determine the laser unit vector in the laboratory coordinate system. We obtain the matrix A used in Eq. (12),

$$A = \begin{pmatrix} 0.0175 & -0.6910 & 0.7226 \\ 0.5863 & 0.5591 & 0.5863 \\ -0.7691 & 0.3805 & 0.5135 \end{pmatrix}$$

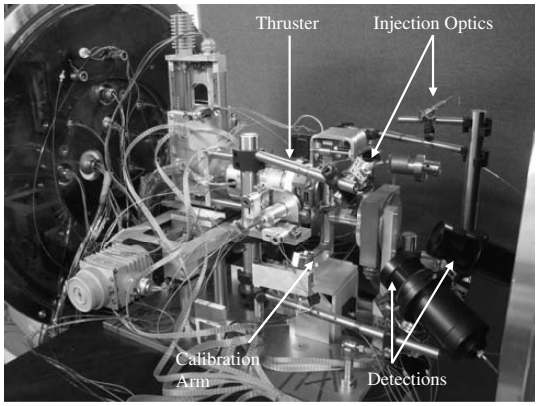

Fig. 11 View of the test bench before its insertion in the B61 vacuum tank.

which gives the following angles between each laser axis:

$$(\widehat{e_1 \cdot e_2}) = 87,3^\circ \qquad (\widehat{e_1 \cdot e_3}) = 84,6^\circ \qquad (\widehat{e_2 \cdot e_3}) = 86,4^\circ$$

The size of the focal point is crucial for the spatial resolution: the smaller the better. This is the reason for the choice of 50 μm optic fiber to direct the laser beams, which, once focused, gives focal points of less than 1 mm in diameter. The laser intensity measured in each beam is about 150 μW. A calibration arm is located in front of the thruster. It holds a charge-coupled-device (CCD) chip and a reference cell containing cesium vapor at saturated vapor pressure. A Pt100 temperature sensor monitors the temperature of this cell. This arm can be stowed or deployed at two locations in front of the thruster to expose either the CCD chip or the reference cell, used for absorption calibration, at the laser beam crossing point. Thus, the crossing of the three focal points, which gives the actual probed volume, is checked in vacuum using the CCD chip mounted on the arm. Two detection optics are used for redundancy and to avoid blind spots. These detection optics are 50 mm lenses with a 25 mm diaphragm. Their focal length is 75 mm. They are mounted on vacuum-rated motorized mounts; thus, they can be aligned while in vacuum. Their alignment with the probed volume is checked with the CCD cell by back-tracking a laser beam. Overall, the probed volume, which is the crossing of the laser beams and the detection optic solid angle, is about 1 mm^3. The fluorescence light collected is focused on 600 μm optic fibers; background light is filtered out using a bandpass filter centered at 850 nm. The fluorescence signal is the directed toward a Hamamatsu R636-10 photomultiplier sensitive in the red part of the spectrum.

The test bench is also equipped with lateral optics for lateral absorption measurements along the X axis in the thruster coordinate system. A neutral density filter (ND3) is used in front of the injection optic to decrease the laser intensity and to thus be in the linear absorption regime. While the thruster is off, the absorption signal can be calibrated; i.e., we measure the T_{Ref} in Eq. (14) using the reference cell, similar to those used in the optical train, mounted directly on the calibration arm. This reference cell, of known cesium vapor pressure, is used to perform a direct calibration of the absorption signal or of the fluorescence signal, in vacuum, at the measurement point location.

Finally, the thruster is mounted on a three-axis orthogonal translation system. The reference of the coordinate system is taken when the probed volume, defined by the crossing of the three probing lasers, touches the center of the emitter slit. When the thruster is switched off and pushed back, the calibration arm can be extended to check the laser beams and detection crossing and to calibrate the absorption.

In the detection stage, all signals are acquired on a National Instrument card at 20 kHz. Before sampling, they go through 10 kHz anti-aliasing filters. These signals are 1) the output of the photomultiplier tube collecting the fluorescence from the vacuum chamber, 2) the of the photomultiplier tube used for the reference LIF in the cesium cell, 3) the laser beam power, and 4) the Doppler-free absorption signal.

C. Measurement Procedure

The measurements are taken for four different operating conditions of the thruster. These conditions are given in the test matrix shown in Table 2.

When the emitter temperature reaches steady state, we start the measurement. First, plane B is probed, then plane C. Each plane is processed line by line; a line is parallel to the X axis. On each line,

Table 2 Test-case matrix

	Emitter temperature	
Thrust	35°C	90°C
30 μN	Case 1	Case 3
100 μN	Case 2	Case 4

Table 3 Characteristics of the planes

	Plane B	Plane C
Position on Z axis	3 mm	9 mm
Width	30 mm	37 mm
Height	12 mm	35 mm
ΔY (spacing between lines)	2 mm	5 mm
ΔX (increment between points)	2–4 mm	3–5 mm
NY (number of lines)	7	8
NX (number of points per line)	9	11
Number of points	63	88
Number of LIF signal required	189	264
Number of absorption signals required	7	8

several point measurements are taken. The number of points and lines and the dimensions of the planes are given in Table 3.

For each measurement point, 30 to 50 frequency sweeps are recorded for each laser. Each frequency sweep is calibrated using the corresponding Doppler-free absorption signal. Then the resulting LIF signals are averaged to increase the signal-to-noise ratio.

For each test case, the calibration of the LIF signal necessary to have the C_1 constant is done once using the centerline on plane C. The constant C_1 is then used to obtain quantitative measurement on both planes. The reason for this choice is that the relative number density profile, sketched in Fig. 9 cannot be fully resolved on plane B, because there are blind spots inside the thruster. Thus, the tails of the profile are unknown and a calibration with a partial relative profile and the absorption signal along this line would be highly inaccurate. On the contrary, on plane C, the relative profile goes to zero at the edges of the measurement plane. Thus, we are confident that there is no cesium outside of the plane. Examples of relative profiles on both planes are shown in Figs. 12 and 13. The drawback of using C_1 obtained from plane C for the measurement on plane B is that it induces a systematic error. This systematic error is due to absorption of the probing laser beam between plane C and plane B.

D. Measurement Performance

The typical uncertainties of the different measured quantities are summarized in the Table 4. Because of self-absorption, the mass flow rate computed from plane B measurements can be underestimated by up to 30%. This uncertainty is treated as a random error in the following.

The measurement resolutions $S(X)$ in our current conditions are given in Table 5. These numbers correspond to the acquisition time (or rather, number of averaged samples) used in our data acquisition.

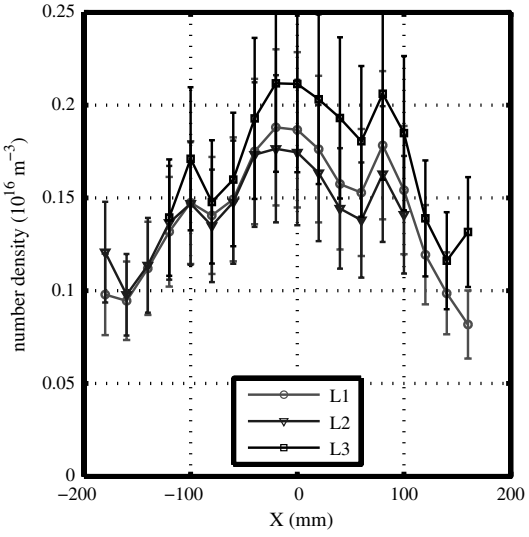

Fig. 12 Cesium number density profile along a line, thrust 30 μN, emitter temperature 35°C, and plane B.

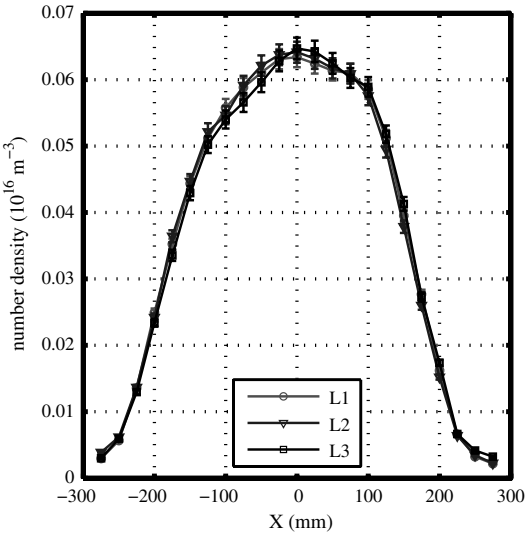

Fig. 13 Cesium number density along a line, thrust 30 μN, emitter temperature 35°C, and plane C.

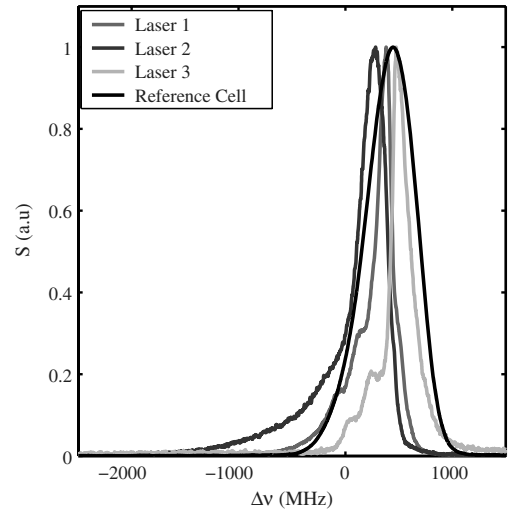

Fig. 14 View of normalized fluorescence signals for the three lasers and the reference cell, on plane C, $X = +20$ mm, $Y = +00$ mm, and case 1.

If more frequency sweeps are taken, the resolution can be increased as the square root of the number of sweeps.

Note that thee absorption has less resolution than the LIF measurement. This is because the absorption measurement noise is largely due to the laser diode intensity fluctuations, which are below 1%. These fluctuations have less impact on the LIF measurement, because the fluorescence signal is not linearly dependent on the intensity.

Table 4 Uncertainties of the different quantities

Measured quantity	Plane B	Plane C
Number density n_{Cs}	10%, plus self-absorption underestimate of <30%	6%
Velocity	5%	5%
Flow rate	<5%, plus self-absorption underestimate of <20 to 30%	<5%

Table 5 Resolution in the conditions of the experiment

Measured quantity X	$S(X)$
Point number density measurement from LIF	10^{-10} m bar $= 2.4 \times 10^{12}$ m^{-3}
Velocity measurement	2 m s^{-1}

V. Results

A. Point and Line Signals

Figure 14 shows the three LIF signals from the three probing lasers L1–L3; the LIF signal from the reference cell is also given. The fluorescence signals of L1 and L2 are shifted toward the red part of the spectrum, which means that the neutral cesium is flowing toward the laser optics or, in other words, the neutral cesium is flowing out of the thruster.

In Fig. 12 (plane B), the three relative density profiles along a line are given. The discrepancies between the curves are due to self-absorption in the high-density plume at this location. Indeed, because the laser and collected light on plane B need to pass through the bulk of the cesium plume, self-absorption introduces a bias in the number density measured in plane B, depending on the laser beam used. This bias results in a 20% uncertainty on the number density, on top of the 10% uncertainty due to random error, as mentioned in Table 4. In Fig. 13 (plane C), the curves are in very good agreement; indeed, self-absorption is much less intense here, because the cesium number density is much lower in this part of the plume. Note that both curves in Figs. 12 and 13 show that the plume is fairly symmetrical.

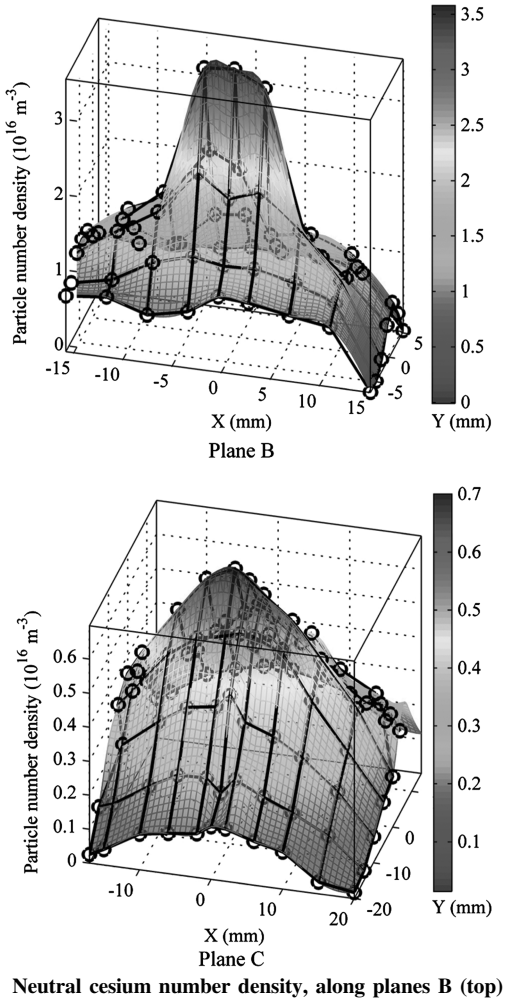

Fig. 15 Neutral cesium number density, along planes B (top) and C (bottom), thrust 30 μN, and emitter temperature 35°C. Measurement points are the nodes of the black mesh, which is spline-interpolated for visualization purpose. Along plane B the number density has an elongated peak, corresponding to the active region of the emitter. The number density does not go to zero at the edge of the measurement plane. Along plane C the plume has a broader shape because of the plume expansion.

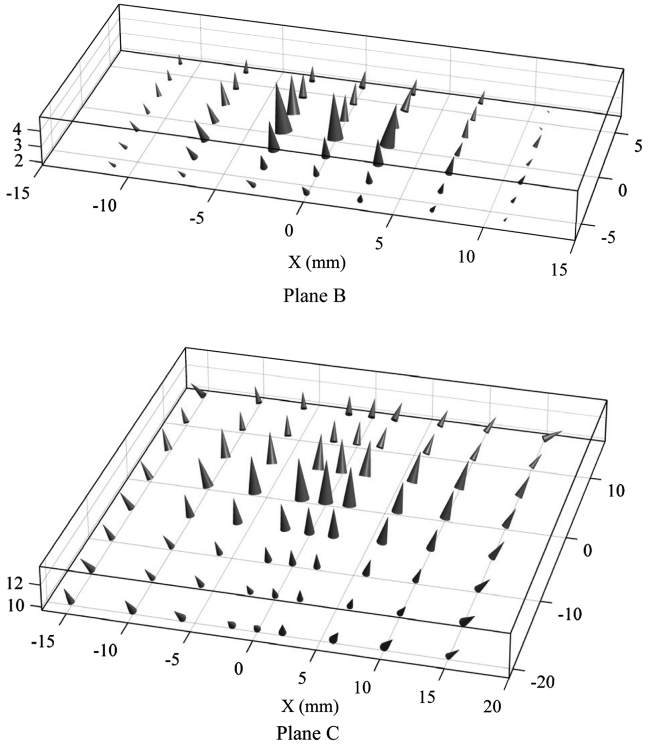

Fig. 16 Velocity vector orientation, along planes B (top) and C (bottom), thrust 30 μN, and emitter temperature 35°C. The size of the vector is proportional to the magnitude of the velocity. The divergence of the beam can be seen from the divergence of the 3-D velocity vectors.

B. Mappings for Case 1

In Figs. 15–18, the mappings obtained on planes B and C for the test case 1 (see Table 2) are shown. In Fig. 15, the number density mappings on both planes are shown. The number density mappings in Fig. 15 show that the number density is the largest at the center of the emitter slit. The evolution between planes B and C shows the broadening of the neutral cesium plume. Similarly, the velocity vector fields in Fig. 16 show that the velocity reaches its maximum at the center. The Z-velocity mappings shown in Fig. 17 indicate that the maximum axial velocity can be as high as 800 and 600 m s^{-1}, on planes B and C, respectively. At higher thrust, the maximum axial velocity can exceed 1000 m s^{-1} on plane B, at the center of the emitter ($X = 0$). Combining the number density mapping and the Z-velocity mapping gives the neutral mass flux mapping, shown in Fig. 18. The mapping on plane B shows that the region of maximum flux has a large aspect ratio, which is consistent with the large aspect ratio of the emitter slit. Since plane B is just 3 mm downstream of the emitter, this shows that the neutral cesium comes from the emitter.

C. Measured Mass Flow Rates

Results similar to those presented above were obtained for the three other cases; from these data the mass flow rate are computed using Eq. (8). In Table 6, we summarize the mass flow rates measured for the four test cases shown in Table 2. For comparison, the mass flow rate resulting from the ion current is indicated. It should be noted that total mass flow rate was not measured directly, as differential mass flow measurements were not accurate enough to provide usable data. In addition, the neutral fractions of the total flow rate reported in Table 6 are computed assuming the ion current was formed by singly charged ions, which is known to not be the case. Using a typical cluster ion fraction as measured in previous experiments would yield significantly lower values of neutral mass flow rate fraction. So the fraction values reported in Table 6 are mainly indicative of the relative change at the different conditions tested and cannot be considered as an absolute measurement.

VI. Discussion

A. Neutral Mass Flow Rate Measurements

The flow rate measurements summarized in Table 6 require a few comments. First, neutral mass flow rate is as high as, or even higher than, the ion mass flow rate. This observation differs markedly from the early results of Mitterauer [2], but is of the same order of magnitude as the results of [3], which take into account the total mass flow rate due to neutrals including droplets. The order of magnitude of our measurements has been checked using absorption measurement, which can be easily calibrated. The high number density is not due to a background cesium accumulation. Spot checks outside of the plume, while the thruster is firing, have shown that the cesium number density is below the detection limit of our setup. Our data show unambiguously that the neutral mass flow rate is not negligible and should be taken into account when determining the propellant mass to store in the thruster unit.

Second, the profiles of mass flux plotted for each plane show that most of the neutral cesium flows through the central part of the measurement planes. This is illustrated, for example, in Fig. 18, in which black curves outline the area accounting for 80% of the total measured flow rate. The presence of this central peak indicates that even though the measurement plane does not cover completely the

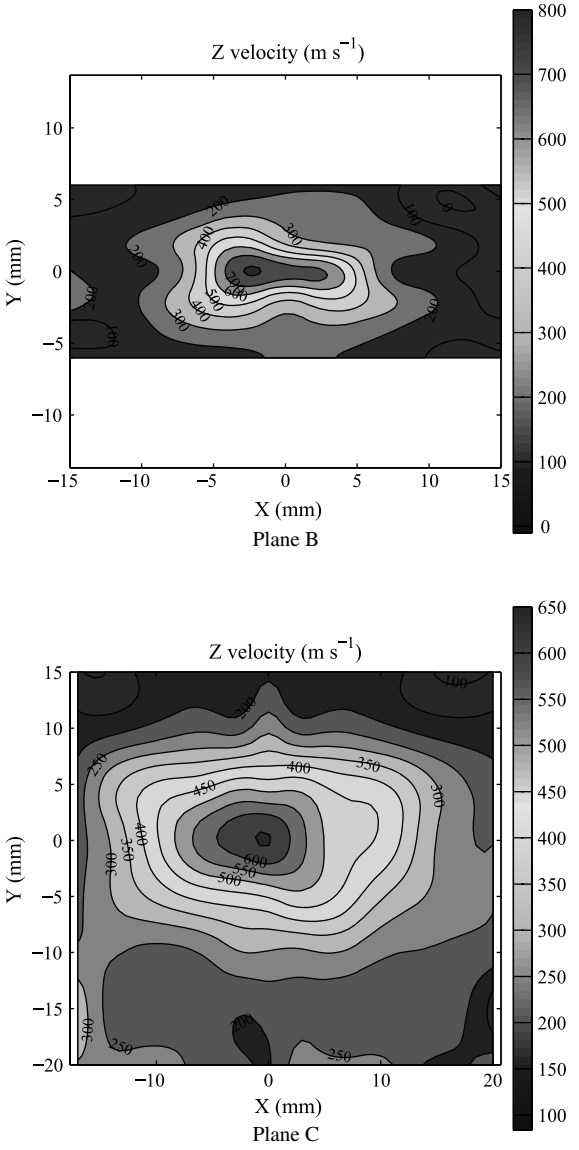

Fig. 17 Z-velocity mapping along planes B (top) and C (bottom), in m s^{-1}, for thrust 30 μN, emitter temperature 35°C. Along plane B, the maximum velocity reach 800 m s^{-1}; the maximum velocity region follows roughly the active region of the emitter.

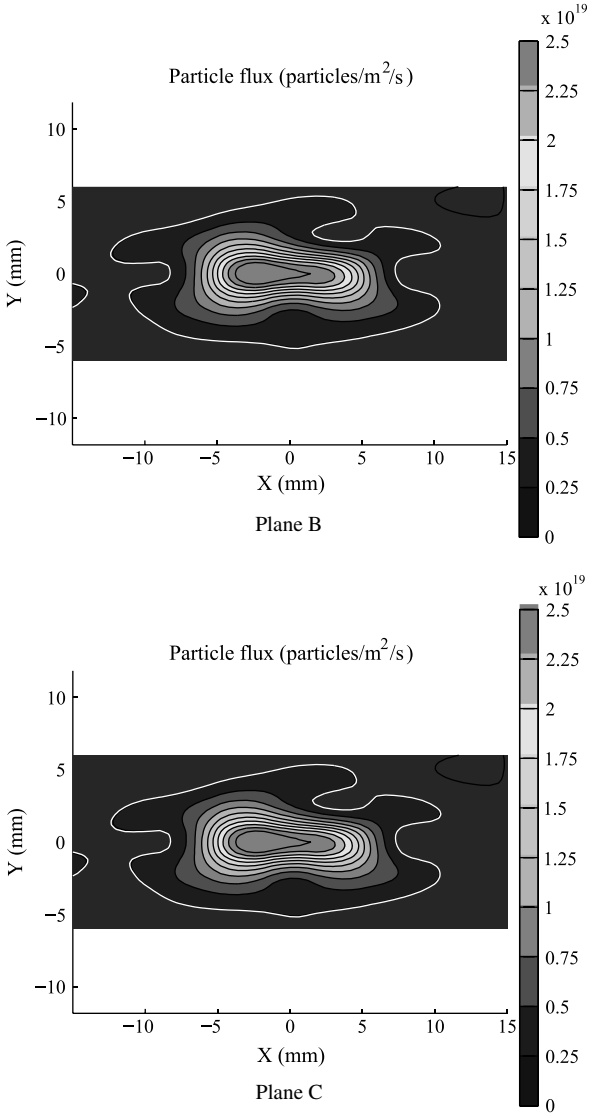

Fig. 18 Particle flux isovalues along planes B (top) and C (bottom); thrust 30 μN, emitter temperature 35°C, given in $m^{-2}\,s^{-1}$. The area enclosed by the white line account for 80% of the total flux.

thruster exit plane (see, for example, Fig. 6), the flow rate obtained should be within 5% of the total mass flow rate.

Third, there is a clear correlation between the emitter temperature and the neutral flow rate. At a given thrust, the higher the emitter temperature, the larger the mass flow rate. Similarly, at a given emitter temperature, the higher the thrust, the larger the neutral cesium atom mass flow rate. As a first approximation, we could decouple the effect of thrust and emitter temperature and suppose that the total neutral mass flow rate is the added contribution of a thermal plume resulting from cesium evaporation and a thrust-dependent plume. Thus, one could write

$$q = q_{\text{Thermal}} + q_T \tag{18}$$

Supposing that the mass flow rate q_T depends linearly on the thrust, i.e., that $q_T = k_T \times T$, we find that $q_{\text{Thermal}} \simeq 0.2$ mg/h, $k_T = 0.033$ mg/h/μN and $q_{\text{Thermal}} \simeq 2.2$ mg/h, $k_T = 0.039$mg/h/μN for emitter temperatures of 35 and 100°C, respectively. The mass flow rate q_{Thermal} due to the thermal plume increases with emitter temperature, which is expected, since the vapor pressure of cesium is a steep function of the temperature (see footnote [††]). Interestingly, the values of k_T are quite close for both temperatures, which suggests that the thermal plume and the thrust-dependent plume are not closely coupled. Because a minimum thrust is needed to operate the thruster in our experiment, a full mapping of the plume with zero thrust has not been done. Instead of full mapping, spot checks at the center of the plume are done at zero thrust, but with constant emitter temperature. These checks show that the cesium number density does not go to zero, whereas the averaged velocity falls to the 100–200 m s^{-1} range.

The underlying physical mechanisms of this thrust-dependent plume can be further discussed by considering the maximum averaged velocities measured. At the center of the plume, the cesium velocity magnitude is about 500–1000 m s^{-1}. At this point, we recall that this is an averaged velocity: i.e., the results of the added contribution of each velocity class. For comparison, the averaged thermal velocity of a cesium vapor at 35°C would be about 220 m s^{-1}, and the maximum averaged velocity resulting from an isentropic expansion would be about 310 m s^{-1}. Thus, there is clearly an effect on the neutral cesium plume that increases its velocity. We can think of three possible causes: 1) acceleration of the neutral vapor by elastic collisions with the fast ions, 2) recombination or charge exchange of cesium ions into fast neutrals in the high number density plasma at the tip of the emitter slit, and 3) evaporation of the cesium vapor from fast-charged clusters.

If the idea of a neutral cesium plume being composed of a thermal plume and a thrust-dependent plume holds, we would then expect a velocity distribution function of the neutral cesium composed of a shifted Gaussian at thermal speed and a high-velocity component responsible for the high averaged velocity. However, extracting velocity distribution function from the LIF spectra is beyond the scope of this study. This would have to be checked in future experiments.

Finally, results of the neutral flow measurement test seem to indicate that the propellant utilization efficiency, also termed mass efficiency (defined as the ratio between nominal singly ionized mass flow of ions and actual overall mass flow) for the thruster has values between 40 and 50% when the thruster is operated at nominal working temperature, which occurs in beginning-of-life conditions. The efficiency can drop to values between 20 and 30% when the

Table 6 Neutral cesium flow rate for the different thruster conditions

Case	1	2	3	4
Thrust, μN	30	100	30	100
T_{emitter}, °C	35	35	90	90
Plane B				
Flow rate, mg/h	1.25 ± 0.42	3.33 ± 1.11	2.36 ± 0.80	4.78 ± 1.60
Fraction of total mass flow rate	53%	49%	65%	58%
Plane C				
Flow rate, mg/h	1.18 ± 0.02	3.41 ± 0.04	3.33 ± 0.05	6.05 ± 0.05
Fraction of total mass flow rate	51%	50%	72%	63%
Ion[a]				
Flow rate, mg/h	1.13	3.46	1.28	3.52
Fraction of total mass flow rate, neutral mass flow of plane C	49%	50%	28%	37%

[a]The ion mass flow rate is computed from the current, supposing singly charged ions. The ratio of neutral cesium or ionized cesium to the total mass flow rate is given in each case.

Table 7 Thrust due to the neutral cesium flow, computed from Eq. (19)

Conditions	Plane	T_x, μN	T_y, μN	T_z, μN	T, μN
		Case 1			
$T = 30$ μN	B	0.014	−0.024	−0.160	0.163
$T_e = 35$°C	C	0.020	−0.019	−0.128	0.129
		Case 2			
$T = 100$ μN	B	0.029	−0.062	−0.616	0.620
$T_e = 35$°C	C	0.022	−0.066	−0.464	0.469
		Case 3			
$T = 30$ μN	B	0.011	−0.022	−0.156	0.159
$T_e = 90$°C	C	0.002	−0.018	−0.192	0.193
		Case 4			
$T = 100$ μN	B	0.040	−0.092	−0.655	0.662
$T_e = 90$°C	C	0.021	−0.059	−0.551	0.555

thruster is operated at high temperature (close to 100°C), which may occur at end of life if the thruster is subject to degradation of electrical performance and a fraction of the power is dissipated inside the unit. These conditions were verified in the frame of two endurance tests performed by Alta and reported in [13]. In both of these tests, the electrical performance of the thruster gradually deteriorated, leading to an increase of the emitter temperature above 120°C. The average mass efficiency was evaluated in both tests by weighing the thruster at the beginning and at the end of the test and then comparing the propellant consumption with the computed total impulse. The calculated mass efficiency was on the order of 20% for both tests (22% for the shorter test and 18% for the longer one), in line with the predictions based on the results of the neutral flow measurements reported in this paper. At present, Alta is working to reduce the electrical performance degradation at end of life, with the aim to improve both power and mass efficiency.

B. Neutral Thrust

It is interesting to note that the emission of cesium atoms results in an additional thrust. In fact, we can compute this additional force with

$$\mathbf{T}_{\text{Neutral}} = -\int [p\mathbf{n} + m_{\text{Cs}} n_{\text{Cs}} \mathbf{V}(\mathbf{V}\cdot\mathbf{n})]\,\mathrm{d}S \tag{19}$$

In Eq. (19) we can verify that the contribution of the cesium pressure p is negligible. If we perform this integration on the probed surfaces (planes B and C), we can compute force in the thruster coordinate system. Note that a fraction of this force, due to fast neutrals produced by charge exchange or fast-charge clusters, is already accounted for in the thrust computed from the ion current. Thus, the total thrust cannot be obtained directly by summing this force and the ion thrust. However, it gives an upper bound for the thrust due to thermal neutral expansion. The results are given in Table 7. In all cases, the thrust caused by the exhaust of the neutral gas is below 1 μN. Figure 19 shows the thrust vector computed from plane B for the four test cases. The tilt angle of the neutral thrust vector is below 8°.

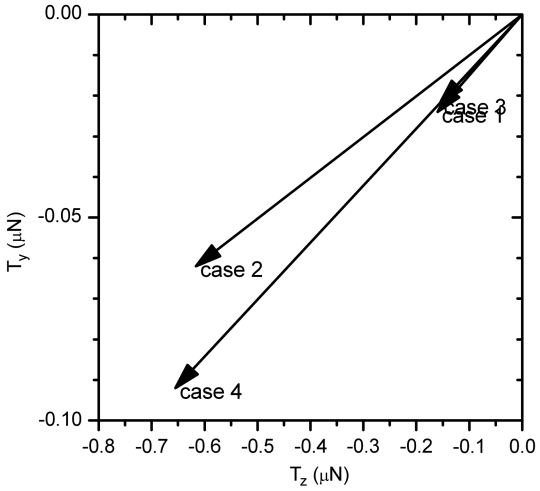

Fig. 19 Neutral thrust vectors in the *Y*–*Z* plane for the four cases. *Y* axis not at scale. Thrust values are negative because of the orientation of the thruster coordinate system. Neutral thrust is mainly axial; the thrust vector is tilted to, at most, 8° with respect to the main thrust axis (*Z* axis).

VII. Conclusions

In this study, for the first time, the mass flow rate of neutral cesium atoms emitted by a cesium FEEP thruster was successfully measured. To achieve this, a nonintrusive optical diagnostic technique based on laser-induced fluorescence was developed. An experimental setup was devised that allows one to measure the three components of neutral cesium velocity, as well as its absolute number density, using absorption spectroscopy as a calibration tool. Using this setup, the neutral number density and the three velocity components of neutral cesium expelled by an engineering model of a FEEP thruster for four different operating conditions were mapped. From these data, the mass flow rate across two control surfaces was obtained. The uncertainty of these measurements can be as low as 5%.

The results show that the neutral cesium mass flow rate is approximately equal to the charged particle mass flow rate. The measured mass flow rates indicate that the plume is composed of a thermal plume, resulting from cesium vaporization, and a thrust-dependent plume. Indeed, axial velocities are in the 600–1000 m s^{-1} range. Even an isentropic expansion cannot account for this magnitude. There could be three mechanisms responsible for this high neutral velocity: elastic collisions with ions, inelastic collisions (recombination) or charge-exchange collision, and vaporization from charged cluster.

This study brings forward some exciting questions that should be investigated. First, what is the mechanism responsible for the fast neutral velocity? A first step to answer this question would be to deconvolve the LIF signal to find the neutral velocity distribution function. Such a procedure would require carefully considering the relative strength of the cesium transitions, as well as the self-absorption effects. A second step would be to obtain not only the projected velocity distributions, but also the full velocity vector distribution function (i.e., in phase space), from which the plume structure could be accurately investigated. For this purpose, probing along three axes is insufficient. A more complex technique is required.

Second, can this technique be extended to probe other species in the plume or other types of thruster? As a first step, it an investigation of the cesium dimers in the plume is proposed. The key point here would be to devise the proper set of transitions that would allow a direct calibration. If such transitions could not be found, other optical diagnostics leveraging the ground state could be used or one could also extend the technique to two-photon laser-induced fluorescence to probe atoms or ions from their ground state.

Acknowledgments

This work was performed under European Space Research and Technology Centre contract 19718/06/NL/HB. The authors acknowledge B. Attal-Tretout, N. Dorval, T. Schmid, and A. Bresson for their support during this study; A. Broc and S. Rocca for their assistance during the experiments; and P.-E. Frigot from ESA for providing additional power supply units.

References

[1] Tajmar, M., and Wang, J., "Three-Dimensional Numerical Simulation of Field-Emission Electric-Propulsion Backflow Contamination," *Journal of Spacecraft and Rockets*, Vol. 38, No. 1, Jan. 2001, pp. 69–78. doi:10.2514/2.3656.

[2] Mitterauer, J., "Field Emission Electric Propulsion: Spectroscopic Investigations on Slit Emitters," ESA, Dec. 1985.

[3] Bartoli, C., von Rohden, H., Thomson, S. P., and Blommers, J., "A Liquid Caesium Field Ion Source for Space Propulsion," *Journal of Physics D: Applied Physics*, Vol. 17, 1984, pp. 2472–2483.

[4] Cedolin, R., Hargus, W., Jr., Storm, P., Hanson, R., and Cappelli, M., "Laser-Induced Fluorescence Study of a Xenon Hall Thruster," *Applied Physics B (Lasers and Optics)*, Vol. 65, No. 4, Oct. 1997, pp. 459–469. doi:10.1007/s003400050297

[5] Dorval, N., Bonnet, J., Marque, J. P., Rosencher, E., Chable, S., Rogier, F., and Lasgorceix, P., "Determination of the Ionization and Acceleration Zones in a Stationary Plasma Thruster by Optical Spectroscopy Study: Experiments and Model," *Journal of Applied Physics*, Vol. 91, No. 8, 2002, pp. 4811–4817. doi:10.1063/1.1458053

[6] Hargus, W. A., and Charles, C. S., "Near Exit Plane Velocity Field of a 200-Watt Hall Thruster," *Journal of Propulsion and Power*, Vol. 24, No. 1, 2008, pp. 127–133. doi:10.2514/1.29949

[7] Hargus, W., Jr., and Cappelli, M., "Laser-Induced Fluorescence Measurements of Velocity within a Hall Discharge," *Applied Physics B (Lasers and Optics)*, Vol. 72, No. 8, June 2001, pp. 961–969.

[8] Smith, T. B., Herman, D. A., Gallimore, A. D., and G. J. W., Jr., "Laser-induced Fluorescence Velocimetry of Xe II in the 30-cm NSTAR-type Ion Engine Plume," AIAA Paper 2004-3963, July 2004.

[9] Williams, G. J., Jr., Smith, T. B., III, F. S. G., Beal, B. E., Gallimore, A. D., and Drake, R. P., "Laser Induced Fluorescence Measurement of Ion Velocities in the Plume of a Hall Effect Thruster," AIAA Paper 99-2424, June 1999.

[10] Cappelli, M., and Hargus, W. H., "VUV Absorption Measurements of Ground State Xenon in the Near Field of a Low Power Hall Thruster," AIAA Paper 2004-4120, July 2004.

[11] Nicolini, D., Frigot, P.-E., Musso, F., Cesare, S., Castorina, G., Ceruti, L., Bartola, F., Zanella, P., Ceccanti, F., Priami, L., and Paita, L., "Direct Thrust and Thrust Noise Measurements on the LISA Pathfinder Field Emission Thruster," 31st International Electric Propulsion Conference, Paper IEPC-2009-183, Ann Arbor, MI, 2009.

[12] Linne, M. A., *Spectroscopic Measurement*, Academic Press, New York, 2002.

[13] Ceccanti, F., Paita, L., Cesari, U., Tata, M. D., Giusti, N., Balducci, P., Pistoia, M. D., Nicolini, D., and Napoli, L. D., "3200 hours Endurance Testing of the Lisa Pathfinder FT-150 Thruster," 31st International Electric Propulsion Conference, Paper IEPC-2009-170, Ann Arbor, MI, 2009.

J. Blandino
Associate Editor